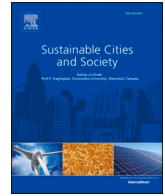




Contents lists available at ScienceDirect

Sustainable Cities and Society

journal homepage: www.elsevier.com/locate/scs

Optimal allocation of local climate zones based on heat vulnerability perspective

Rui Zhang^a, Jun Yang^{a,b,c,*}, Xinyue Ma^a, Xiangming Xiao^d, Jianhong (Cecilia) Xia^e

^a Urban Climate and Human Settlements Research Lab, Jangho Architecture College, Northeastern University, Shenyang 110169, China

^b Human Settlements Research Center, Liaoning Normal University, Dalian 116029, China

^c School of Humanities and Law, Northeastern University, Shenyang 110169, China

^d Department of Microbiology and Plant Biology, Center for Earth Observation and Modeling, University of Oklahoma, Norman, OK 73019, USA

^e School of Earth and Planetary Sciences (EPS), Curtin University, Perth 65630, Australia

ARTICLE INFO

Keywords:

Urban thermal environment
Optimization methods
Population
Thermal adaptation
Shenyang city

ABSTRACT

Global climate change presents considerable heating risks to cities, necessitating the assessment of heat vulnerability characteristics in urban areas for the advancement of human settlements and socioeconomic progress. Nevertheless, there has been a lack of extensive research regarding heat vulnerability when considering local climate zones (LCZs). In this study, we utilized data from multiple sources to construct a model for evaluating heat vulnerability along three dimensions: Exposure, Sensitivity, and Adaptability. We analyzed the spatial characteristics of heat vulnerability in the LCZs and employed a linear weighted multi-objective optimization method to reconfigure the LCZs and mitigate the Urban Heat Vulnerability Index (HVI). The findings revealed that (1) The spatial characteristics of exposure and sensitivity were similar, with high values observed in the city center and low values at the periphery. Adaptability exhibited a high–low–high pattern from the center to the edge due to the combined influence of the economy and natural factors. (2) The HVI of the built environment (building LCZ) surpassed that of the natural environment (natural LCZ) within the research area. Specifically, compact high-rise buildings (LCZ1) and compact midrise buildings (LCZ2) accounted for over 90% of the area with extremely high and high HVI values, necessitating immediate optimization efforts. (3) By considering the area and population size of the research area, we achieved an optimal heat vulnerability plan by increasing the areas of LCZ4 and LCZA while reducing the areas of LCZ8 and LCZ1, among others. Therefore, the overall HVI of the study area decreased from 49,034.67 to 41,772.37, representing a reduction of 14.81 %. This study presents an innovative approach to mitigating urban heat vulnerability, providing valuable planning references and scientific guidance to assist cities in addressing high-temperature risks.

1. Introduction

Global climate change has intensified, leading to frequent heat waves and exacerbated urban heat island (UHI) effects (Russo et al., 2014; Spinoni et al., 2015). The expansion of impermeable surfaces due to rapid urbanization, coupled with increased energy consumption from human activities, has contributed to rising temperatures (Tuholske et al., 2021). Elevated temperatures pose risks to human health, increasing the likelihood of diseases and fatalities (Sun et al., 2014; Ebi et al., 2021; Yang et al., 2021b). In 2003 alone, persistent summer heat waves caused over 70,000 deaths in Western Europe (Sun et al., 2022). Certain vulnerable populations experience heightened health risks due to the combined effects of heat waves and heat islands (Li et al., 2015;

Mohammad Harmay and Choi, 2022). Studies indicate that heat risks will continue to escalate in the future (Dong et al., 2015).

Urban residents are particularly susceptible to extreme weather events and global climate change, with the geographical characteristics and economic levels of cities often playing a moderating role (Yazar et al., 2022). The United Nations Sustainable Development Goals (SDGs) recognize climate change as a crucial aspect of achieving sustainable development. Consequently, understanding the thermal characteristics and influential factors within cities is fundamental to mitigating high-temperature risks and enhancing the comfort of living environments. In urban climate research, compared with traditional meteorological observation methods, remote sensing methods can be employed to obtain massive amounts of image data with high spatial and temporal

* Corresponding author at: Urban Climate and Human Settlements Research Lab, Jangho Architecture College, Northeastern University, Shenyang 110169, China.
E-mail address: yangjun8@mail.neu.edu.cn (J. Yang).

<https://doi.org/10.1016/j.scs.2023.104981>

Received 20 June 2023; Received in revised form 16 August 2023; Accepted 30 September 2023

Available online 1 October 2023

2210-6707/© 2023 Elsevier Ltd. All rights reserved.

resolution, which can be used to calculate land surface temperatures (LSTs), classify land usage, and survey natural disasters, and can be applied in other fields (Huang et al., 2020; Liu et al., 2021b; Schwaab et al., 2021). GIS methods can be employed to conduct spatial analysis of geographical big data such as points of interest (POI) and mobile phone signaling (Pappalardo et al., 2015), and evaluate their interactions with urban thermal environments by establishing mathematical models (Zhi et al., 2020). Creating spatial distribution maps of heat risks using remote sensing and geographic big data can effectively support planners in devising urban optimization and cooling strategies (Tomlinson et al., 2011; Jiang et al., 2015; Zhou et al., 2021; Renc et al., 2022; Chen et al., 2023a).

The concept of local climate zones (LCZ), proposed by Oke et al., describes similar climate states found in complex cities (Oke and Stewart, 2012; Stewart et al., 2014). Due to structural, land use, and metabolic similarities among LCZs, they can have comparable influences on the local climate. This classification is widely applicable in various countries and regions for investigating the connection between urban surface characteristics and temperature, making it a commonly used approach in the study of urban thermal environments (Gardes et al., 2020). The LCZ concept can be utilized to calculate the urban heat island intensity (UHII) and overcome the binary urban–rural limitations associated with traditional methods (Han et al., 2022; Chen et al., 2023b). LCZs are characterized by variations in UHI intensity and spatial and temporal patterns (Yang et al., 2018). For instance, the UHII of built-up LCZs tends to be higher than that of natural LCZs (Cai et al., 2021). Moreover, the UHI effect is more likely to occur on clear and cloudless nights (Yang et al., 2018; Chang et al., 2021).

Furthermore, several studies have focused on the spatiotemporal characteristics and driving factors of temperature differences between LCZ classes (Yang et al., 2020b; Chang et al., 2021; Lemoine-Rodriguez et al., 2022). These interclass differences are related to geographical characteristics, land use, landscape metrics, urban morphology parameters, human activities, and other factors (Li et al., 2022b; Wu et al., 2022; Zhou et al., 2022). Research has demonstrated that bare soil and paved roads significantly contribute to land surface temperature (LST) (Yang et al., 2021a), while high-density and compact building types generally exhibit higher LST values compared to low-density and open building types (Yang et al., 2019; Li et al., 2021). Additionally, studies have explored the thermal and environmental impacts of different LCZs, such as changes in vegetation phenology (Kabano et al., 2021), energy consumption characteristics (Kotharkar et al., 2022), and variations in subjective thermal perception (Leconte et al., 2015; Lau et al., 2019). The interactions between LCZs and other urban climate fields, such as heat waves and wind environments, have also been extensively discussed (Giannaros et al., 2022; Li et al., 2022a; Zhang et al., 2022). In summary, LCZs can serve as a means to express the spatiotemporal distribution characteristics of the urban thermal environment and facilitate the exploration of driving factors and impacts of temperature changes. These studies provide comprehensive insights into the relationship between LCZs and the urban thermal environment. However, few studies have combined LCZs with heat vulnerability frameworks.

The heat vulnerability framework serves as a comprehensive thermal index that quantifies the impact of high temperatures on cities and assesses the potential damage they may face when exposed to heat risks (Karanja and Kiage, 2021). Vulnerability is a widely utilized concept in various fields, including environmental pollution, disaster management, and engineering science (Aroca-Jimenez et al., 2020; Sabrin et al., 2020). The specific aspects of vulnerability vary across different domains (Ford et al., 2018). In the IPCC4, heat vulnerability encompasses three dimensions: exposure, sensitivity, and adaptability (IPCC, 2007; Inostroza et al., 2016). Exposure is measured by the proximity of individuals or urban systems to high-temperature disasters, sensitivity reflects the susceptibility of individuals or urban systems to such disasters, and adaptability refers to the capacity of individuals or urban systems to adapt and withstand potential or existing high-temperature

pressures by modifying their states and behaviors (Ellena et al., 2020). IPCC6 emphasizes the interdependence and mutual influence between different systems in terms of vulnerability (IPCC, 2022).

Studies on heat vulnerability have examined the spatial and temporal heterogeneity within the study area by calculating relevant parameters (Nayak et al., 2018). Administrative regions are commonly employed as units for effective data collection and statistical analysis, often serving as the preferred scale for heat vulnerability research (Chen et al., 2022b). The use of remote sensing and geographic big data has facilitated research at smaller scales, enabling a more accurate understanding of the spatial distribution characteristics of heat vulnerability (Ho et al., 2018; Sun et al., 2022). Moreover, studies have investigated factors influencing heat vulnerability (Ho et al., 2018; Xiang et al., 2022), disparities among cities of different levels (Estoque et al., 2020), and the impact of heatwave interactions on human populations (He et al., 2019). These studies have deepened our understanding of the principles and connections between heat vulnerability and urban systems, providing valuable insights for urban governance and optimization.

The integration of LCZ and the heat vulnerability framework in research is comprehensive, as it explicitly establishes connections among LCZs, the thermal environment, urban socio-economy, and other factors, thereby offering valuable insights for urban planners in decision-making processes. Chen et al. have emphasized the urgent need for addressing heat risks associated with densely populated medium to high-rise buildings (Chen et al., 2022a). Heat risk characteristics within LCZs in Beijing reveal that open low-rise LCZs exhibit the largest thermal risk area, open midrise LCZs accommodate the highest population at risk, and lightweight low-rise LCZs have the highest proportion of thermal risk areas (Zhou et al., 2021). However, few studies have been conducted on this specific topic. Furthermore, the practical implementation of research findings in spatial planning, particularly regarding the allocation of LCZs to mitigate the Heat Vulnerability Index (HVI), has not been extensively explored. Earlier studies have demonstrated that utilizing LCZs for planning and regulation purposes can effectively reduce LST. Yi et al. discovered that converting LCZ2 and LCZ3 into LCZ4 and LCZ6 would result in a temperature decrease of 1–3°C (Yi et al., 2022). Yang et al. optimized the area layout of LCZs to reduce heat island intensity based on the thermal environment characteristics of Dalian City (Yang et al., 2020a). Therefore, our study proposes a scheme to calculate the HVI of LCZs and mitigate heat effects through optimized LCZ configuration.

In this study, our objective is to construct a heat vulnerability model and elaborate on the statistical results and spatial distribution characteristics of exposure, sensitivity, and adaptability from the LCZ perspective. Furthermore, we employ optimization methods to reconfigure LCZs and propose a new scheme for reducing the HVI. By quantifying both the change in LCZ areas and the resulting reduction in HVI, our study aims to provide more effective assistance in urban design and planning decision-making. The ultimate goal is to mitigate urban thermal risks and enhance the comfort of urban living environments.

2. Data and Methods

2.1. Data source

This study conducted a comprehensive analysis of multiple data sources, including remote sensing, vectors, points of interest (POI), and socioeconomic statistical data. The attributes and sources of the data are listed in Table 1. The division of LCZ categories in the study area was based on WUDAPT map data (Demuzere et al., 2022), as depicted in Fig. 2. The overall classification accuracy (OA) of the research area was 74.611%. The meaning and individual classification accuracy of each type of LCZ (OAC) are shown in Table 2.

For the remote sensing analysis, Landsat 8 imagery data from August 2, 2018, were selected and pre-processed to account for atmospheric

Table 1
Data sources and descriptions.

Data	Description	Source
LCZ classification data	100 m	http://www.wudapt.org/wudapt/
Landsat 8	30 m/100 m	https://earthexplorer.usgs.gov/
Luojia-1	130 m	http://59.175.109.173:8888/index.html
POI	Vector point data	https://www.amap.com/
OSM	Vector line data	http://www.openstreetmap.org
Population	100 m	https://www.worldpop.org/
Statistical data	Table Data	http://tjj.shenyang.gov.cn/
Auxiliary data	Vector surface data	https://www.webmap.cn/

Table 2
LCZ classification accuracy for different categories.

LCZ	Description	OAc
LCZ 1	Compact high-rise	64.469 %
LCZ 2	Compact mid-rise	59.838 %
LCZ 3	Compact low-rise	58.312 %
LCZ 4	Open high-rise	63.667 %
LCZ 5	Open mid-rise	59.500 %
LCZ 6	Open low-rise	64.171 %
LCZ 8	Large low-rise	76.172 %
LCZ 9	Sparsely built	60.461 %
LCZ 10	Heavy industry	56.444 %
LCZ A	Dense trees	81.043 %
LCZ B	Scattered trees	57.229 %
LCZ D	Low plants	84.616 %
LCZ E	Bare rock or paved	88.000 %
LCZ F	Bare soil or sand	70.180 %
LCZ G	Water	93.867 %

absorption and reflection through atmospheric correction. Night light (NL) intensity was measured using Luojia 1 data, which provided a higher spatial resolution compared to the Defense Meteorological Satellite Program (DMSP) and National Polar-orbiting Partnership (NPP) data. To cover the entire research area, we selected three similar images obtained during the summer of 2018, and NL data were obtained based on cropping and splicing. The density of socioeconomic activities and medical services was analyzed using POI and OpenStreetMap (OSM) data. Population distribution grids and statistical data were utilized to correct the actual population density in the study area. Additionally, auxiliary data such as administrative division data were employed to support the analysis. Based on the detailed data, this study constructed a framework for a heat vulnerability model and explored the characteristics of the HVI in the study area from an LCZ perspective.

2.2. Methods

2.2.1. Construction of a heat vulnerability index model

The heat vulnerability framework consists of three dimensions: exposure, sensitivity, and adaptability. In this study, based on previous research findings and the characteristics of Shenyang city, 10 factors were selected to construct the framework, including Land Surface Temperature (LST). The exposure dimension comprises LST as the sole factor. The sensitivity dimension encompasses five factors: Population Density (PD), density of economic activities (POI1 and POI2), Road Density (RD), and Normalized Difference Building Index (NDBI). The adaptability dimension includes four factors: Night Light intensity (NL), density of medical facilities (MD), Normalized Difference Vegetation Index (NDVI), and Modified Normalized Difference Water Index (MNDWI).

The detailed definitions and calculation methods for each factor are provided below.

- (1) LST: The LST was calculated by inverting data from Landsat 8, which accurately reflects the thermal spatial distribution of the study area and serves as a representative factor for heat exposure. Atmospheric correction methods were employed based on the principle of thermal radiation balance (Qin et al., 2001). This approach removes the impact of atmospheric radiation transfer, allowing for the accurate calculation of surface radiation information and subsequent determination of LST.

$$L_{\lambda} = [\epsilon B(T_s) + (1 - \epsilon)L_1]\tau + L_{\uparrow} \tag{1}$$

$$B(T_s) = [L_{\lambda} - L_{\uparrow} - \tau(1 - \epsilon)L_1] / \tau\epsilon \tag{2}$$

$B(T_s)$ represents the brightness of black-body radiation. ϵ denotes the surface-specific radiance, while τ the atmospheric transmittance in the thermal infrared band. L_{\uparrow} represents the upward radiation brightness from the atmosphere, and L_1 represents the energy reflected from the atmosphere and reaching the ground as downward radiation.

By using the Planck formula, T_s as shown in formula (3):

$$T_s = K_2 / \ln(K_1 / B(T_s) + 1) \tag{3}$$

Atmospheric profile parameters can be obtained from NASA, while the surface-specific radiance can be obtained using the NDVI threshold method. The Landsat 8 data, in conjunction with the LST inversion tool encapsulated in the ENVI extension tool, allows for the retrieval of LST.

- (2) PD: The PD represents the degree of population aggregation. The extent of harm and risks faced by individuals from high temperatures is greater when more people are affected. In this study, demographic data from 2018 was used to revise the global population grid data and accurately calculate the population distribution in the study area. The calculation formula is as follows (4):

$$Pd = \alpha \cdot Pop \tag{4}$$

α is the correction coefficient, which can be derived from the Shenyang Statistical Yearbook. "Pop" represents the population count of the 100 m grid for the global population in 2018.

- (3) Economic activity density: High temperatures can have a significant impact on socioeconomic activities, increasing human labor costs and potentially causing shutdowns. To measure sensitivity, we calculated the kernel density of the POI categories associated with socioeconomic activities.

Kernel density analysis, based on POI data, quantifies the distribution density of various socioeconomic activities. The search radius determines the spatial range used in density calculations. If the search radius is small, the resulting kernel density will be uneven and contain significant noise. Conversely, if the search radius is too large, the kernel density will become excessively smooth, leading to a loss of detail. Therefore, selecting an appropriate search radius is critical. In this study, we used Silverman's empirical rules to calculate the search radii for different types of POIs. The formula for calculating the kernel density is shown in Eq. (5).

$$Density = \frac{1}{r^2} \sum_{i=1}^n \left[\frac{3}{\pi} \left(1 - \left(\frac{d_i}{r} \right)^2 \right)^2 \right] \tag{5}$$

$Density$ is the nuclear density. where $i = 1, \dots, n$ is the input point, r is the search radius, and d_i is the distance between point i and the position, where $d < r$.

After the kernel density calculation, principal component analysis

was performed to analyze the spatial distribution characteristics of socioeconomic activities. The results indicate that the first and second components contain over 95 % of the information, and therefore, they were selected as descriptive factors for the distribution characteristics of spatial facilities, namely POI1 and POI2.

- (4) RD: RD represents the distribution of roads within the study area and is calculated as the ratio of the total length of roads to the area of the plot.

$$RD = \frac{L_i}{A_i}, i \in (1, 2, 3, \dots, n) \quad (6)$$

Where L_i is the length of the road in region i , and A_i is the land area in region i .

- (5) NDBI: NDBI reflects the degree of building coverage (Zha et al., 2003). The calculation method is shown in Eq. (7):

$$NDBI = \frac{SWIR - NIR}{SWIR + NIR} \quad (7)$$

where, SWIR is the reflectance value in the shortwave infrared band, taken as the 6th band of Landsat 8, and NIR is the reflectance value in the near-infrared band, taken as the 5th band of Landsat 8.

- (6) NL: NL data are used to indicate the economic development of the research area. There is a high correlation between GDP and nighttime lighting, and an increase in income is beneficial for residents to cope with high temperatures by purchasing refrigeration facilities and air conditioning. Therefore, NL was used as a factor in the adaptability dimension. We used data from Luojia-1 and converted its DN value into a radiance value to represent the economic status of the study area. The higher the NL value, the better the economic development, as shown in Eq. (8).

$$NL = DN^{3/2} \cdot 10^{-10} \quad (8)$$

Where NL is the radiance value after absolute radiation correction, and DN is the grayscale value of the image.

- (7) MD: The density of medical facilities was calculated using the POI data, and the calculation formula is shown in Eq. (5).
- (8) NDVI: NDVI can be used to measure vegetation growth and richness. Research has shown that vegetation has a cooling effect in cities. Places with more vegetation have stronger resistance to high temperatures. Therefore, NDVI was selected as one of the parameters in the adaptability dimension (Tucker et al., 1985). The formula is shown in Eq. (9). The NDVI values range between -1 and 1, and the closer the value is to 1, the lush the vegetation of the pixel.

$$NDVI = \frac{NIR - RED}{NIR + RED} \quad (9)$$

NIR is the reflectance value in the near-infrared band, taken as the fifth band of Landsat 8, and RED is the reflectance value in the red band, taken as the fourth band of Landsat 8. The calculation results were obtained using the ENVI 5.3 toolbox.

- (9) MNDWI: MNDWI was calculated using Landsat 8 and can be used to measure the distribution of water bodies (Xu, 2006). Water bodies have a certain cooling effect that can improve environmental comfort. The formula is shown in Eq. (10):

$$MNDWI = \frac{GREEN - MIR}{GREEN + MIR} \quad (10)$$

GREEN is the reflectance value in the green light band, taken as the third band of Landsat 8, and MIR is the reflectance value in the mid-infrared band, taken as the tenth band of Landsat 8.

Having performed the respective calculations, each factor was re-sampled to a resolution of 100 m. The data attributes of each indicator in the corresponding dimension were all positive, indicating that the larger the value, the higher the evaluation of that dimension. A normalization method was used to eliminate the influence of different units using the formula shown in Eq. (11) as follows:

$$X_{nom} = \frac{X - X_{min}}{X_{max} - X_{min}}, \quad (11)$$

where X_{nom} is the normalized value, and X , X_{min} , and X_{max} represent the original, minimum, and maximum values, respectively.

The values obtained of all assessed indices lie within the range of 0 to 1. The normalized image of each indicator is shown in Fig. 1. For example, LST_N represents the results of LST normalization.

2.2.2. Calculation of the heat vulnerability index

To date, no set of standard variables has been established for calculating the HVI, and consequently, in terms of methodology, the general trend adopted is to assign the same weight to all indicators (Karanja and Kiage, 2021). Calculation of the HVI typically involves one of two methods, namely, the equal weight and the non-equal weight methods (El-Zein and Tonmoy, 2015; Guo et al., 2019). The non-equal weight method involves assigning different weights to individual indicators, which can be determined based on techniques such as expert scoring and the analytic hierarchy process (Estoque et al., 2020; Song et al., 2020). In contrast, the equal-weight method assigns equal importance to each indicator (Tomlinson et al., 2011; He et al., 2019; Chen et al., 2022a). For each dimension, the equal weight addition method can objectively and evenly measure the impact of each parameter with respect to that dimension. The non-equal weight square approach is, however, more susceptible to subjective influences or is associated with difficulty in explaining the values of weights. Accordingly, in this study, we opted to employ the equal-weight method for calculating the HVI, using Eqs. (12) to (14).

$$Expo = LST \quad (12)$$

$$Sen = Avg(\text{Pop} + \text{POI1} + \text{POI2} + \text{RD} + \text{NDBI}) \quad (13)$$

$$Adp = Avg(\text{NL} + \text{MD} + \text{NDBI} + \text{MNDWI}) \quad (14)$$

The definitions and calculation methods corresponding to parameters such as LST and POP are as shown in Section 2.1.

HVI is calculated and mapped using a superposition model, based on the addition and subtraction of the exponents of exposure, sensitivity, and adaptability. Exposure and sensitivity both contribute to an increase in the HVI, whereas adaptability emphasizes a reduction in the degree. Accordingly, the exposure and sensitivity dimensions are added and the adaptability dimension is subtracted to obtain the final HVI. A comprehensive calculation of HVI is performed using Eq. (15) as follows:

$$HVI = Expo + Sen - Adp, \quad (15)$$

where Expo, Sen, and Adp are the heat exposure, sensitivity, and adaptability dimension indices, respectively.

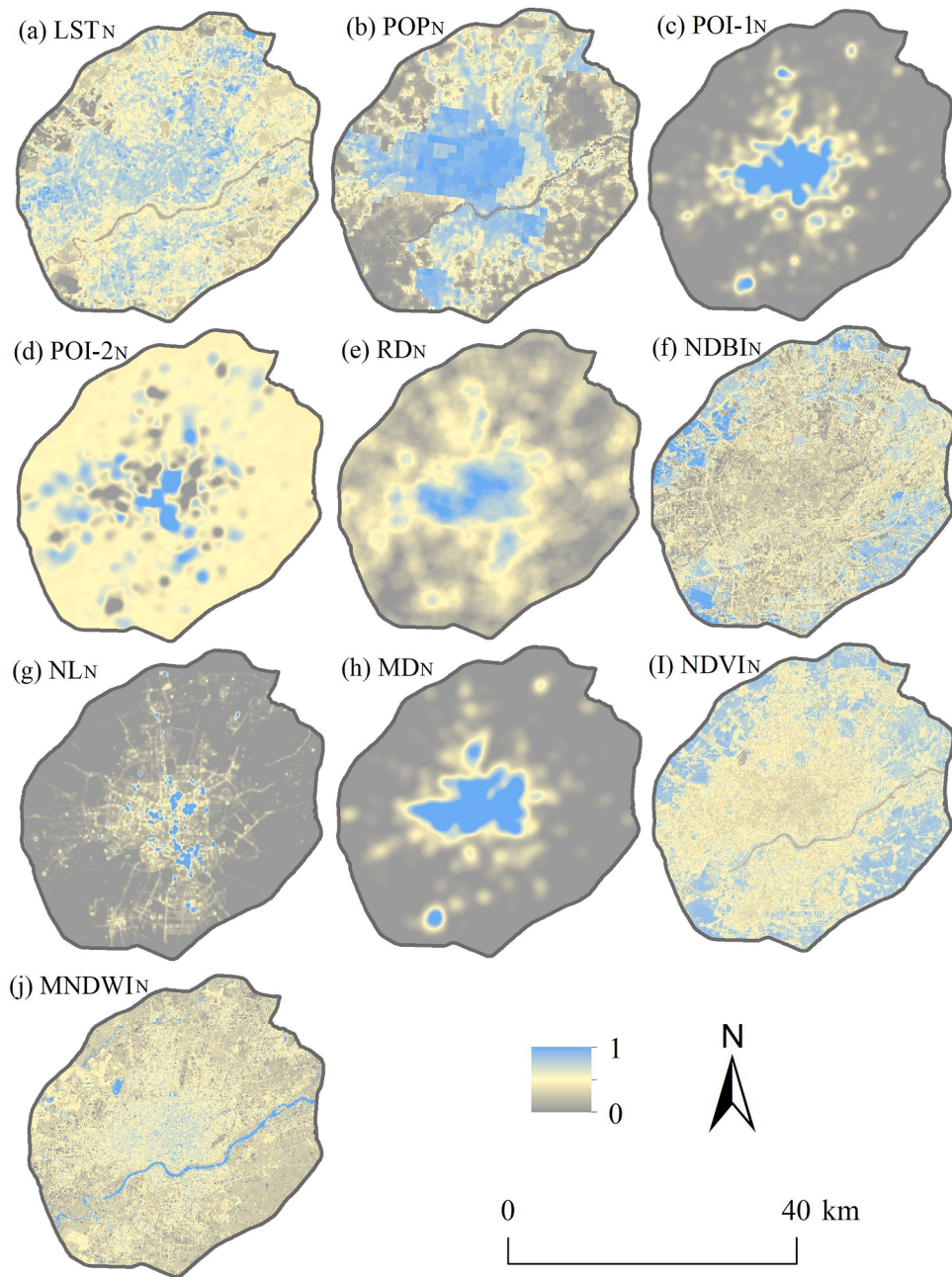


Fig. 1. Ten factor normalized spatial distribution. a. Exposure dimension; b–f, Sensitivity dimension; g–j, Adaptability dimension.

2.2.3. Optimization method

The current distribution patterns of LCZs in cities may contribute to a higher level of heat vulnerability. To address this issue, optimization methods can be employed to reconfigure the LCZ areas and reduce the HVI. Optimization methods are widely applicable across various fields and involve finding the minimum value of a function, known as the objective function. In addition to minimizing the function value, certain fixed conditions, referred to as constraints, must be satisfied. In the optimization process of LCZ configuration, the objective function $f(x)$ aims to minimize the HVI, while the optimized result must adhere to specific conditions, such as population, which serve as constraints. Therefore, the mathematical model for optimizing the allocation of LCZs in the research area can be abstracted as follows:

$$\min f(x) = \sum_{i=1}^n a_i x_i \tag{16}$$

$\min f(x)$ is the minimum sum of the HVI in the study area, x_i is the number of grids in the i th LCZ, a_i is the average HVI corresponding to the i th LCZ;

The basic constraints are:

$$\text{s.t.} \begin{cases} \sum_{i=1}^n c_i x_i \geq b \\ x_j \geq m_j \end{cases} \tag{17}$$

c_i represents the average population of the i th LCZ, and b is the total population of the study area. This constraint condition indicates that the optimized LCZ should accommodate a population greater than or equal

to the total population before optimization. m_j represents the theoretical minimum area of the j th LCZ type, indicating that certain LCZ types, such as green spaces and water bodies, should not decrease during the optimization process. To solve this mathematical model, the Lingo 18 software was utilized. Lingo software, developed by the LINDO Corporation in the United States, is a powerful tool for solving optimization problems (LINDO Systems, 2023). Its built-in solver allows for fast and comprehensive optimization analysis.

2.3. Study area

Shenyang City (122°25"–123°48"E, 41°12"–43°2"N) is located in a region of northeastern China that is predominantly characterized by plains and hills. The region has a temperate semi-humid continental climate with four distinct seasons. The average annual precipitation is approximately 500 mm, the majority of which falls during the summer season. Of the four seasons, summer is the hottest in Shenyang. For the analysis of heat vulnerability in the study area in 2018, we used a combination of remote sensing, geographical big data, and social statistical data. The study area encompasses the land within the 4th Ring Road of Shenyang, covering an area approximately 1233.56 km², and has a permanent population of approximately 5,970,000 individuals. The region serves as the central hub for the economic, political, cultural, and financial activities in Shenyang, which is reflected in a high-density distribution of buildings. Furthermore, the study area encompasses a range of land cover types and is characterized by a complex thermal environment that extends from the urban core to the suburbs. The specific location and extent of the study area are depicted in Fig. 2.

3. Results

3.1. Characteristics of exposure-sensitivity-adaptability under LCZ

The study area was analyzed to calculate the spatial and statistical characteristics of the Exposure-Sensitivity-Adaptability dimensions within the LCZs. The corresponding results are presented in Figs. 3 to 5. Overall, there are similarities in the spatial distribution of the exposure and sensitivity dimensions, while differences can be observed in the adaptability dimension. Each dimension exhibits distinct characteristics in different LCZs.

Fig. 3a illustrates the spatial distribution of exposure, showing a central area with high values surrounded by lower values but with a dispersed pattern. In addition to the concentrated high exposure in the central region, there is another independent high-value area in the southern region. Areas with high heat exposure are found in regions with high economic activity and population density, such as the central area, Shenbei New Area, and Hunnan New Area, as well as areas with developed industrial production, such as Tiexi District in the southwest. The LCZ types of vegetation and water bodies often exhibit low values. A statistical analysis based on the LCZ was conducted, and the corresponding box plot is shown in Fig. 3b. Generally, the average level of heat exposure is higher in built-up LCZs compared to natural LCZs. Among the different LCZ types, LCZ2 has the highest average heat exposure (0.567). Within the built-up LCZs, midrise buildings have higher heat exposure than high-rise and low-rise buildings, and the compact LCZ category exhibits higher heat exposure compared to other types. Among the natural types, water bodies have the lowest thermal

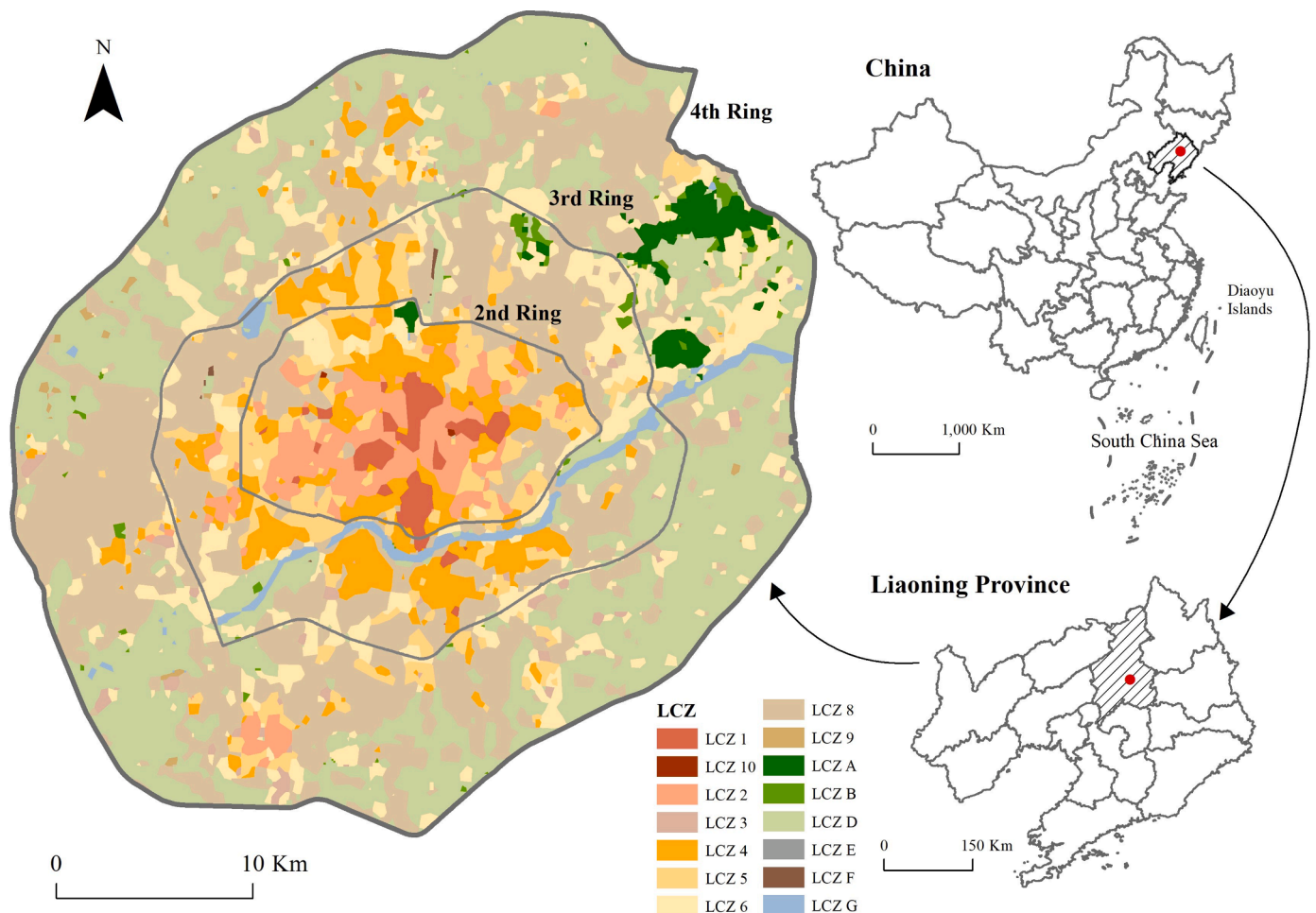


Fig. 2. Study area and LCZ classification map.

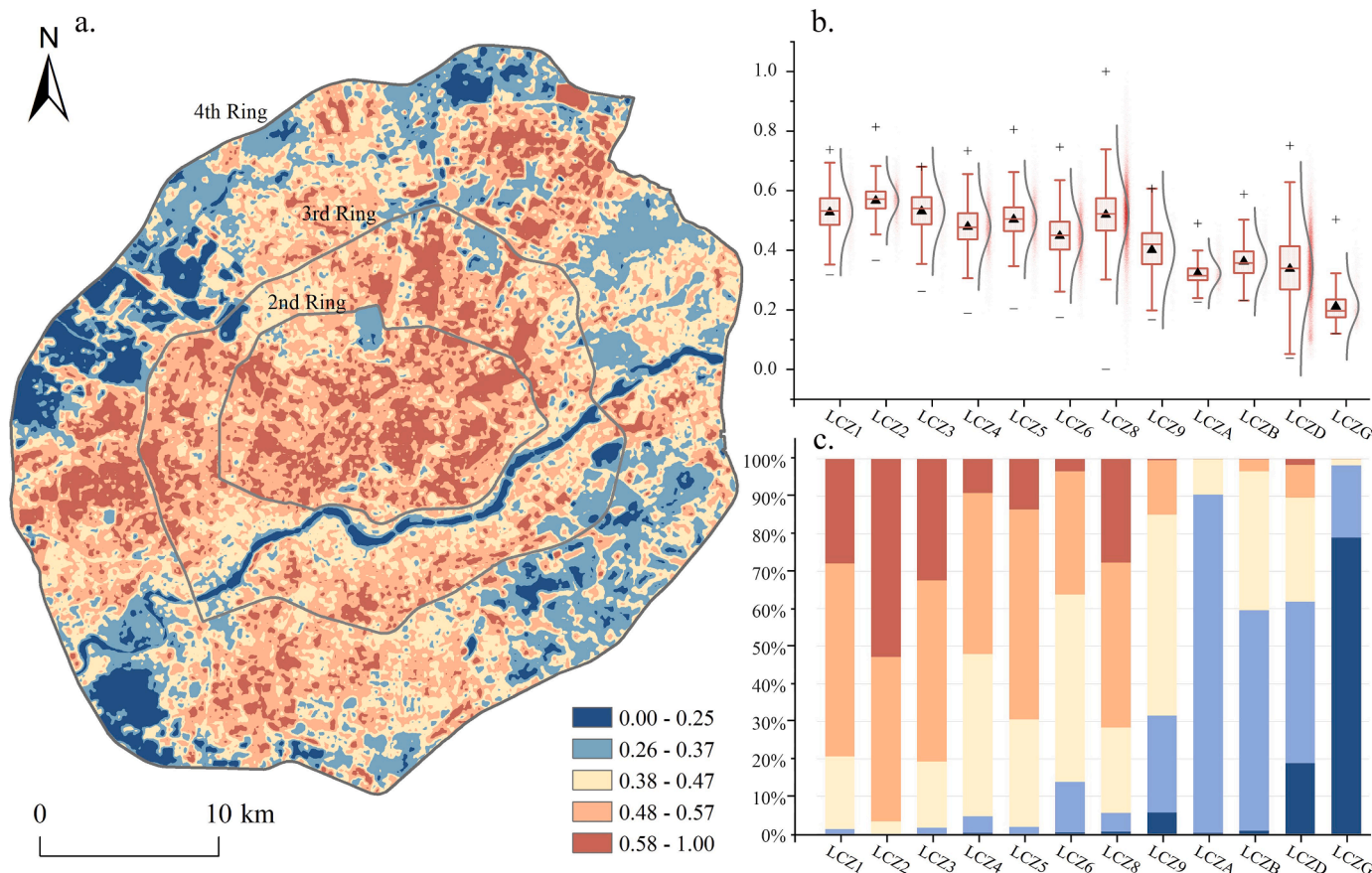


Fig. 3. Exposure features.

a. Map depicting the heat exposure spatial distribution; b. Box plot of statistical characteristics under LCZ; c. Bar chart of Different Levels under LCZ.

exposure (0.212). Fig. 3c presents the levels of heat exposure in each LCZ determined using the Jenks method, which reveals that most of built-up LCZs are rated at 0.38–0.47 or above, indicating severe heat exposure.

The sensitivity dimension is depicted by its spatial distribution in Fig. 4a, showing a central area with high values that gradually decrease toward the surrounding regions in a circular pattern. The sensitivity distribution exhibits a relatively concentrated pattern.

Fig. 4b illustrates that the average heat sensitivity in building LCZs is higher compared to most natural LCZs. Among the natural LCZs, LCZG exhibits the highest sensitivity (0.224), surpassing some building LCZs such as LCZ6 (0.220) and LCZ9 (0.205). These differences in sensitivity can be attributed to the distribution of water bodies in the study area, which covers regions with high population and socioeconomic intensity. Among natural types, the thermal sensitivity of green spaces is lower than that of water bodies, with LCZA having the lowest value (0.158). In terms of building LCZs, midrise and high-rise buildings have higher sensitivity than low-rise buildings. Among the building types at the same height, higher building density corresponds to higher sensitivity. LCZ9 exhibits the lowest heat sensitivity among the building types.

Fig. 4c reveals that fewer LCZs have higher sensitivity values, with the majority falling into the low or moderate levels. This indicates that high sensitivity values are more concentrated compared to heat exposure values.

The spatial distribution representing the adaptability dimension is displayed in Fig. 5a. The central region demonstrates the highest adaptability value, while the surrounding areas exhibit a decreasing trend followed by an increasing trend. The lowest value is observed in a circular area between the edge and center of the study area. Regions with high adaptability are observed in both the northwestern and

southwestern parts of the study area. This distribution pattern arises from interactions between natural and artificial factors. In the central region, better economic conditions enable the development of more effective methods to combat high temperatures. Conversely, the most marginal region demonstrates higher adaptability due to favorable natural conditions. Consequently, areas with the lowest adaptability are situated in the central region characterized by poor economic conditions and a degraded natural environment that cannot withstand high temperatures.

Fig. 5b highlights a significant disparity in the thermal adaptability among the LCZs. Midrise and high-rise LCZs exhibit higher adaptability compared to natural LCZs, while low-rise LCZs have lower adaptability. Specifically, LCZ2 (0.383) and LCZ1 (0.365) demonstrate the highest heat adaptability, surpassing LCZ5, LCZ4, LCZA, and LCZD, whereas these four LCZ categories exhibit slightly higher adaptability than the remaining LCZ types. Fig. 5c illustrates that the majority of LCZs fall within the middle to lower range of adaptability levels.

3.2. Heat vulnerability index features of local climate zones

The HVI values for the study area were calculated using the equal weight addition method, which yielded values within a range between -0.23 and 1.14. To categorize the HVIs, we employed the Jenks method, on the basis of which, the values were grouped in five levels, namely, Very High (0.60–1.14), High (0.46–0.59), Medium (0.30–0.45), Low (0.12–0.29), and Very Low (-0.23–0.11), as illustrated in Figs. 6 and 7. Fig. 6 shows the spatial distribution characteristics of the different levels of HVI. The distribution of the HVI corresponds to the patterns observed for heat exposure and sensitivity. The central region exhibits a concentration of Very High HVI values, while the Very Low HVI values are

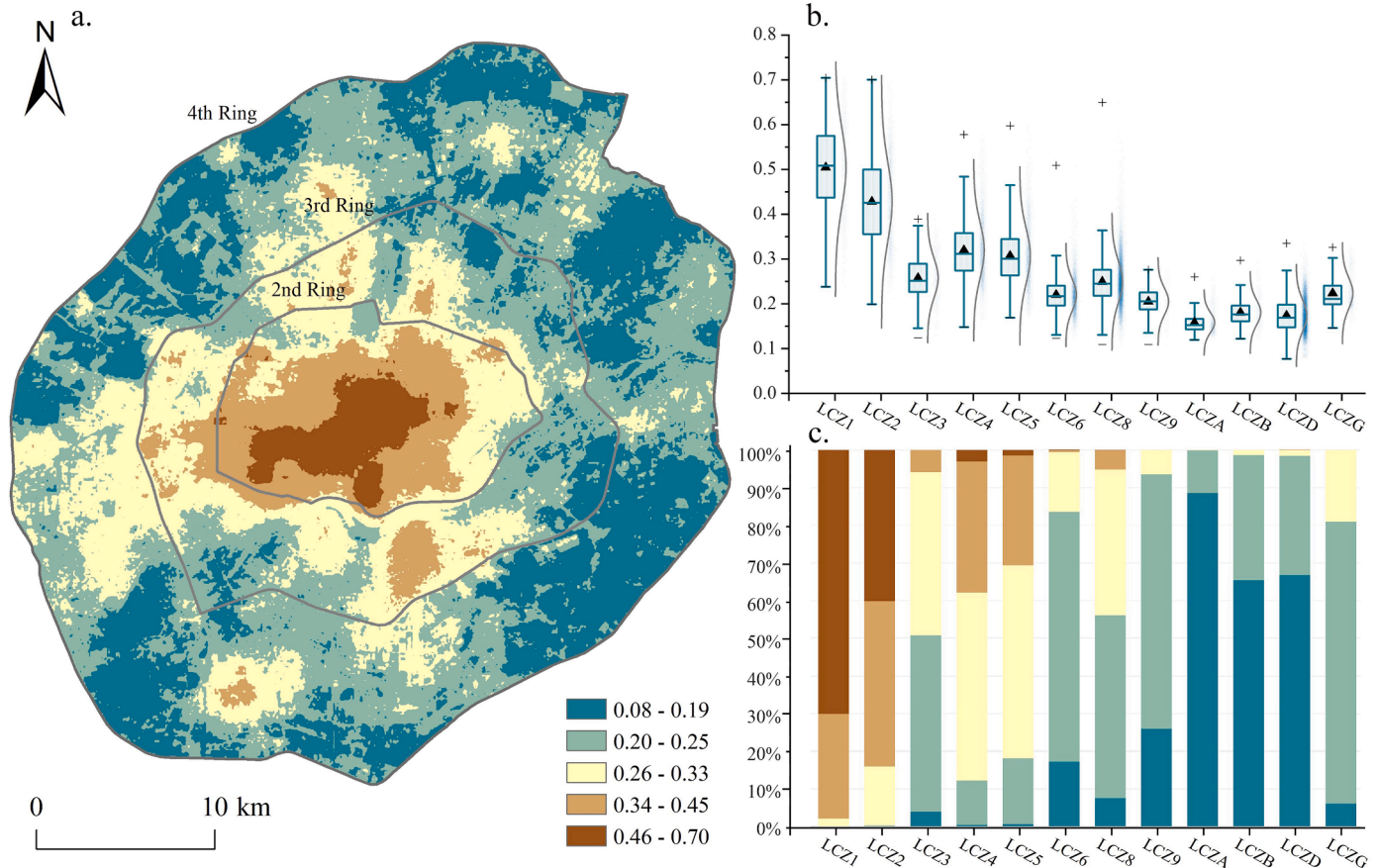


Fig. 4. Sensitivity features.

a. Map depicting the heat sensitivity spatial distribution; b. Box plot of statistical characteristics under LCZ; c. Bar chart of Different Levels under LCZ.

predominantly found at the periphery of the research area, distant from the center.

The statistical characteristics of the HVI for each type of Local Climate Zone (LCZ) were computed using partition statistics, as summarized in Table 3. All building LCZs exhibited higher HVIs compared to the natural LCZs. The average rankings of HVI were as follows: LCZ1 (0.668) > LCZ2 (0.612) > LCZ3 (0.536) > LCZ8 (0.515) > LCZ5 (0.501) > LCZ4 (0.491) > LCZ6 (0.396) > LCZ9 (0.352) > LCZB (0.247) > LCZD (0.216) > LCZA (0.177) > LCZG (0.167). Among the LCZs, the compact types exhibited higher HVI values compared to the open types. The maximum HVI value was observed in LCZ8 (1.137), while the lowest value was observed in LCZD (-0.226).

Fig. 7 presents the distribution proportion of the HVI across various LCZs, revealing significant variations. Building LCZs show a considerable proportion classified as Very High, High, and Medium levels of HVI, while natural LCZs have a larger proportion categorized as Low and Very Low HVI levels. LCZ1 and LCZ2 exhibit over 90% of their area with Very high and High HVI levels. There is a similarity in HVI distribution between LCZ1 and LCZ2, as well as between LCZ4 and LCZ5. The differences between the middle and high floors are relatively small, but notable disparities are observed when compared to the low floors. In LCZ8, the distribution proportions of Very High, High, and Medium HVI levels are similar, and it exhibits the highest standard deviation among all the LCZs, indicating significant internal variations in HVI.

3.3. Optimization of LCZ configuration

Table 4 illustrates the characteristics of LCZs before and after optimization using linear weighted multi-objective optimization. The columns provide specific information about the LCZs. "Pop_1" indicates the

average population of each LCZ type in the grid, while "HVI" represents the average HVI for each LCZ type. "Area_1" represents the LCZ area before optimization, and "Area_2" represents the optimized area. The "Area Ratio" shows the change in the LCZ area. "Pop_2" represents the total population included in each LCZ type after optimization, and the "POP Ratio" indicates the population change ratio before and after optimization. Before optimization, the overall HVI was 49,034.67, while after optimization, it decreased to 41,772.37, indicating a reduction of 14.81%.

Columns 2–4 in Table 4 depict the initial conditions before optimization, adhering to the following criteria: (1) The total population should exceed the pre-optimization value of 5,978,150; (2) The HVI should be minimized after optimization; (3) LCZ types that contribute to urban ecological balance, such as green spaces and water bodies (LCZA, LCZB, LCZD, LCZG), can only increase and not decrease; high heat vulnerability LCZ types (LCZ1, LCZ2) should only be reduced, not increased. Considering the geographical characteristics of the research area, the growth of water bodies was limited to a maximum of three times their initial area.

The last four columns provide the optimized results and a comparison of the changes. The optimization process revealed that among the building LCZ types, only LCZ4 and LCZ5 experienced an increase in area, while the other types saw a decrease. LCZ4 exhibited the most significant increase, with the largest proportion of change, expanding from 88.530 to 201.867 km², representing a 128% increase. LCZ8 experienced the most substantial reduction, shrinking from 404.170 to 143.117 km², reflecting a decrease of 64.6%. In contrast, the natural LCZ types generally experienced an increase in area. LCZA witnessed the most substantial growth, expanding from 20.070 to 127.160 km², representing an impressive increase of 633.6%. LCZD also experienced a

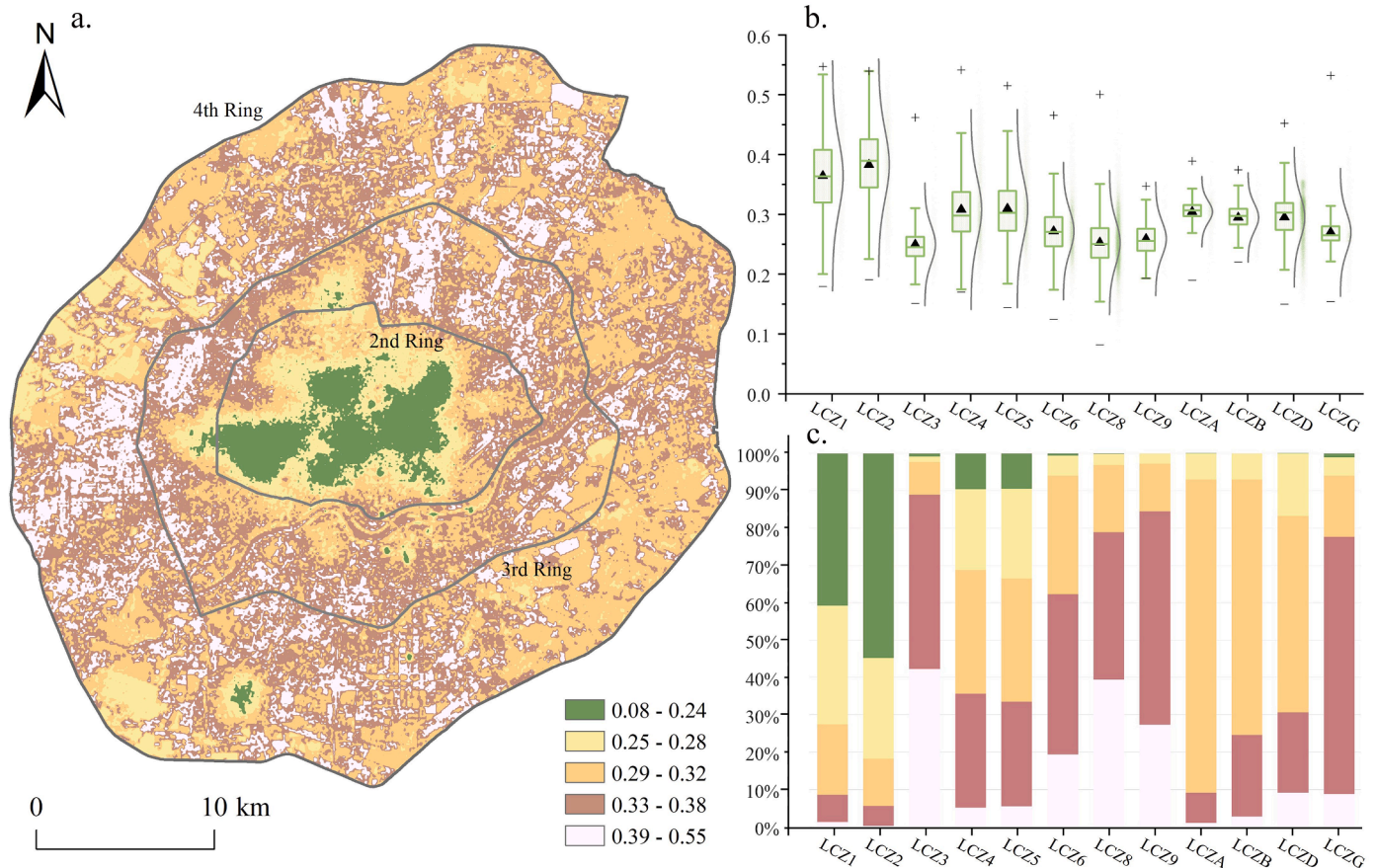


Fig. 5. Adaptability features.

a. Map depicting the heat adaptability spatial distribution; b. Box plot of statistical characteristics under LCZ; c. Bar chart of Different Levels under LCZ.

notable increase, expanding from 384.990 to 453.658 km², although it had the lowest growth rate among the natural types, increasing by only 17.84 %.

After the optimization process, noticeable changes occurred in the population distribution characteristics of the LCZs. Fig. 8 presents these changes using a waterfall chart, offering a visual representation of the population shifts in different building LCZ types before and after optimization. Initially, the population was evenly distributed among LCZ1, LCZ2, and LCZ8, with a balanced distribution across the various LCZ types. However, after optimization, significant disparities in population distribution among the different LCZ types emerged, with LCZ4 now accommodating the highest population.

LCZ1 and LCZ2, both categorized as high heat vulnerability types, successfully reduced their populations, thus mitigating the negative impact of heat vulnerability. In contrast, LCZ4 demonstrated the capacity to accommodate a moderate population while maintaining a moderate level of heat vulnerability, making it one of the most suitable LCZ types for residential purposes.

4. Discussion

4.1. Model parameter selection

The impact of high temperatures on urban areas is often quantified through the construction of comprehensive heat indices. However, these indices typically focus on different aspects, resulting in a lack of complete unification. Given that the selection of different parameters for the construction of HVI may result in inconsistent results, it is necessary to examine the significance of each parameter for the heat vulnerability model. For the purposes of this study, we selected 10 factors to construct

a heat vulnerability model based on three specific selection criteria, namely, that these factors (1) conform to the definition of thermal vulnerability sub dimension, (2) have been scientifically proven through previous research, and (3) meet the needs of the study area.

The exposure dimension, analogous to the “hazard” dimension in heat risk models, includes elements related to temperature, surface temperature, and other relevant meteorological parameters (Chen et al., 2018; Estoque et al., 2020; Liu et al., 2021a). It can also encompass phenomena such as heat waves and heat island intensity (Song et al., 2020; Li et al., 2022a). Parameters within this dimension are commonly derived from observational meteorological data, remote sensing data, and simulation outputs. In this study, we have chosen remote sensing inversion of Land Surface Temperature (LST) as a parameter due to its extensive coverage and ability to capture spatial heterogeneity.

The sensitivity dimension encompasses two primary aspects: physiological sensitivity and socioeconomic sensitivity (Chen et al., 2022b; Sun et al., 2022). The former refers to the different responses of urban residents to high temperatures associated with physiological differences, such as gender, age, and race (Inostroza et al., 2016; Nayak et al., 2018). This also includes the number of individuals who may be affected by high temperatures and the extent of these effects, which are measured in terms of population density (Chen et al., 2022b; Sun et al., 2022). Socioeconomic sensitivity pertains to the susceptibility of urban systems to disruption or damage caused by high temperatures. When the density of social activities increases, the losses incurred due to high-temperature-induced shutdown and production stoppage will also increase, thereby resulting in an increase in HVI. Consequently, parameters, such as employment rates, road density, and building distribution can be used to characterize socioeconomic sensitivity (He et al., 2019). As parameters of socioeconomic sensitivity, we selected road

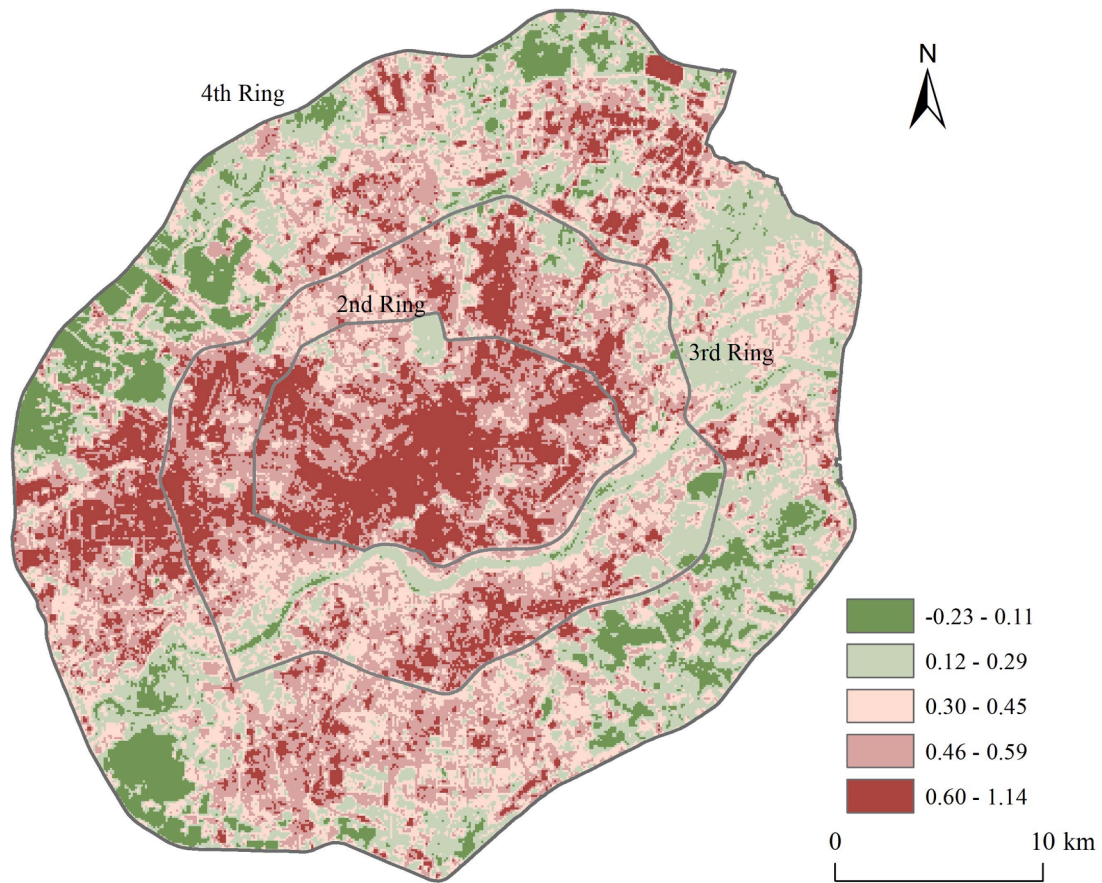


Fig. 6. Map depicting the HVI spatial distribution features.

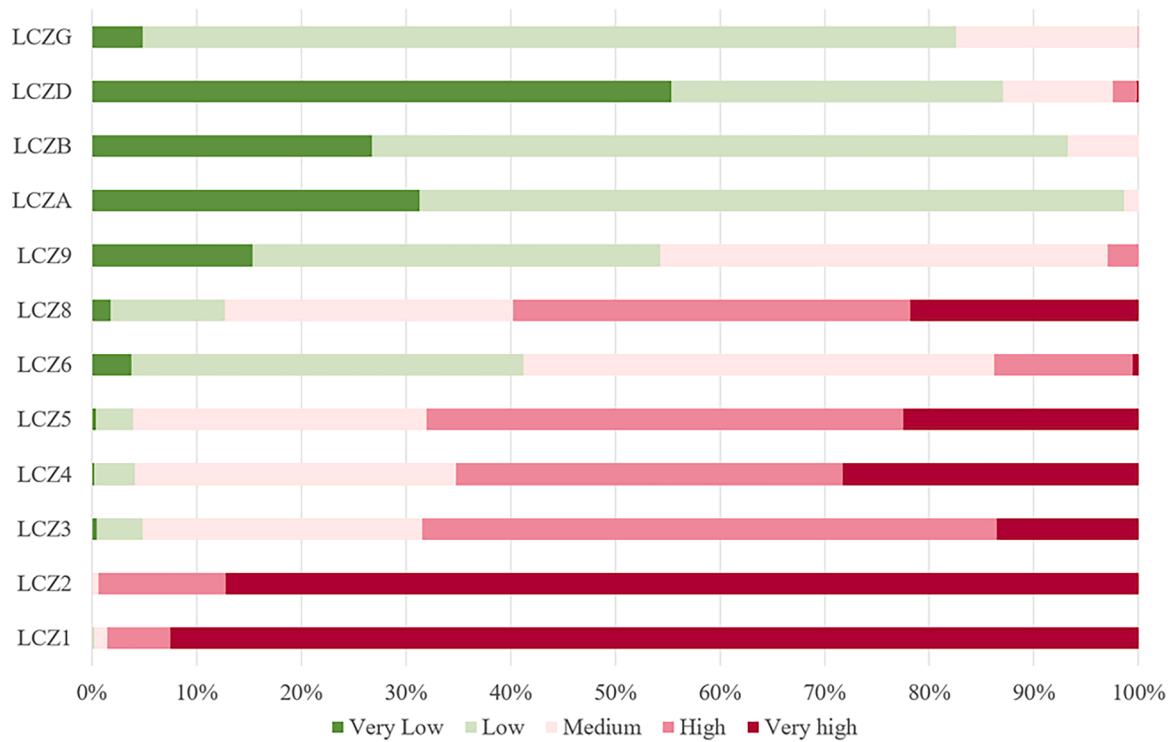


Fig. 7. Bar chart of different levels HVI under LCZ.

Table 3
HVI statistical features of LCZ.

LCZ	Area(km ²)	MIN	MAX	RANGE	MEAN	STD
LCZ 1	17.490	0.230	1.003	0.772	0.668	0.111
LCZ 2	50.410	0.271	0.975	0.705	0.612	0.084
LCZ 3	10.950	0.062	0.813	0.751	0.536	0.106
LCZ 4	88.530	0.085	0.891	0.806	0.491	0.098
LCZ 5	83.140	0.067	0.866	0.800	0.501	0.094
LCZ 6	141.750	-0.034	0.850	0.883	0.396	0.110
LCZ 8	404.170	-0.088	1.137	1.225	0.515	0.137
LCZ 9	2.520	-0.020	0.657	0.677	0.352	0.118
LCZ A	20.070	0.071	0.536	0.465	0.177	0.059
LCZ B	7.470	0.048	0.576	0.528	0.247	0.085
LCZ D	384.990	-0.226	0.786	1.012	0.216	0.166
LCZ G	17.420	-0.016	0.552	0.569	0.167	0.075

density, POI density, and NDBI in the present study.

The adaptability dimension primarily focuses on the cooling capacity of the environment and additional resources derived from socioeconomic development and planning regulations (Sun et al., 2022). This dimension incorporates factors such as the distribution of green spaces and water bodies, the density of cooling facilities (e.g., air conditioning), the proximity to medical resources, and the level of economic development (Fischer et al., 2022; Wang et al., 2023). Better economic conditions and more reasonable urban planning can contribute to reducing the harmful effects of high temperatures. For example, groups with higher incomes are more likely to have access to cooling facilities, and nighttime lighting data has been shown to be highly correlated with GDP. We accordingly selected nighttime lighting data as an adaptation parameter. Areas with dense medical facilities are also more likely to receive assistance in response to high temperature hazards. The distribution of green spaces and water bodies helps to reduce urban temperatures (Du et al., 2017; Peng et al., 2020). Therefore, NL, MD, NDVI, and MNDWI were selected as indicators for the adaptability dimension.

4.2. Differences in optimization results under various constraints

During the optimization process, we established a set of constraints with the goal of minimizing the HVI. The primary constraint was to maintain a constant total population and total area before and after optimization. In addition to these fundamental constraints, we introduced advanced constraints that imposed limitations on the area changes of specific LCZs and the overall rate of area change in the study area. These advanced constraints were gradually incorporated as the optimization process progressed. This section focuses on the variations in LCZ optimization results under different constraints, highlighting the necessity of including advanced constraint conditions.

Under the basic constraints, the optimal allocation of LCZs can be treated as a linear programming problem. The nature of linear programming dictates that the optimal value occurs at a critical point. In our study area, the minimum HVI obtained was 21,572, although this

Table 4
Comparison of LCZ before and after optimization.

	Pop_1	HVI	Area_1	Area_2	Area Ratio	Pop_2	Pop Ratio
LCZ 1	386	0.668	17.490	13.952 ↓	-0.202	538547	-0.202
LCZ 2	250	0.612	50.410	40.328 ↓	-0.200	1008200	-0.200
LCZ 3	44	0.536	10.950	0.000 ↓	-1.000	0	-1.000
LCZ 4	128	0.491	88.530	201.867↑	1.280	2583894	1.280
LCZ 5	110	0.501	83.140	120.278↑	0.447	1323057	0.447
LCZ 6	24	0.396	141.750	26.720 ↓	-0.812	64127	-0.812
LCZ 8	33	0.515	404.170	143.117↓	-0.646	472287	-0.646
LCZ 9	16	0.352	2.520	0.000 ↓	-1.000	0	-1.000
LCZ A	6	0.177	20.070	147.235↑	6.336	-	-
LCZ B	8	0.247	7.470	29.495 ↑	2.948	-	-
LCZ D	6	0.216	384.990	453.658↑	0.178	-	-
LCZ G	7	0.167	17.420	52.260 ↑	2.000	-	-

solution was not feasible in practice. Handling this minimum solution involved maximizing the areas of LCZ1 and LCZA to achieve the highest population and the lowest HVI (as shown in Table 5). However, this change resulted in all residents residing in LCZ1 experiencing an extremely high HVI. It is important to note that this mathematical solution represents an optimal outcome only in theory and cannot be practically implemented.

Therefore, it is crucial to refine the constraint conditions to establish a closer relationship with actual urban planning. Firstly, we introduced a new objective, referred to as Object 2, which aims to minimize the change in the LCZ area. This is in addition to the existing objective of minimizing the Heat Vulnerability Index (HVI), referred to as Object 1. Secondly, to reduce the number of residents living in areas with extreme thermal vulnerability within the study area, we forcibly decreased the areas of LCZ1 and LCZ2 by 20 %. By incorporating these new optimization objectives and advanced constraints, the original single-objective linear programming function transformed into a multi-objective nonlinear programming problem.

There exists a tradeoff between Object 1 and Object 2, making it unattainable to simultaneously achieve their minimum values. To visualize the relationship between these variables, a scatter plot was used, as shown in Fig. 9. The relationship between the variables is nonlinear. By employing a linear weighted optimization approach, we

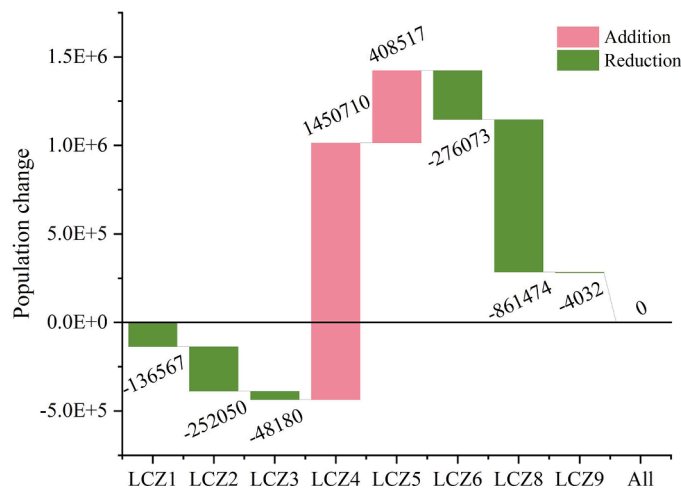


Fig. 8. Waterfall diagram of LCZ population change after optimization.

Table 5
LCZ area at the lowest HVI (km²).

	LCZ1	Other Building LCZ	LCZA	LCZB	LCZD	LCZG
Area	140.500	0.000	678.790	7.470	385.420	17.420

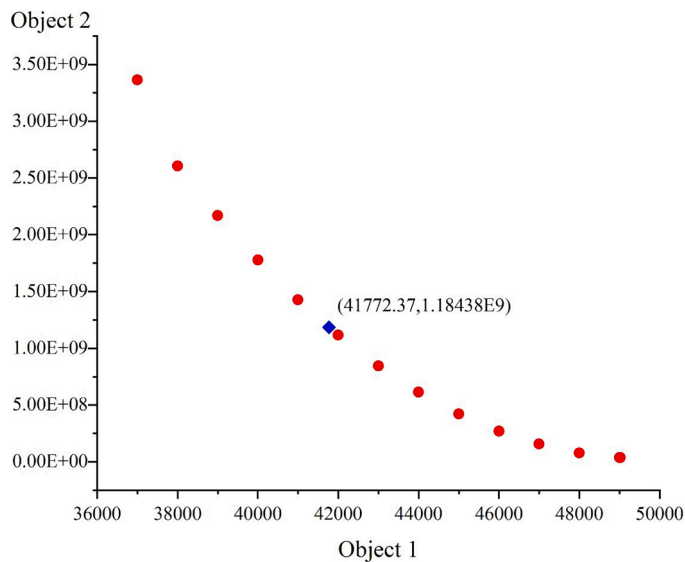


Fig. 9. Scatter plot of function objective value distribution.

were able to balance the values of the two objectives, leading to the determination of the optimal distribution scheme of LCZs and the HVI, represented by the blue dot in Fig. 9.

Based on the aforementioned research, the strategy for reducing urban heat vulnerability from an LCZ perspective involves two approaches. The first approach focuses on directly reducing the HVI of specific LCZs, particularly LCZ1 and LCZ2, which have higher HVI values. The HVI is positively correlated with the exposure and sensitivity dimensions and negatively correlated with adaptability. Consequently, reducing LST and increasing vegetation and water bodies have emerged as viable means of local adjustments (Wu et al., 2021; Renc et al., 2022). The second approach entails modifying the layout of LCZs, decreasing the prevalence of LCZ types with higher HVI and increasing the presence of LCZ types with lower HVI, thus achieving the optimization of urban heat vulnerability—an objective central to our study. Compared to Path 1, the practical implementation of Path 2 may be more intricate, requiring comprehensive research on urban planning to update the LCZ. However, its interpretability and quantifiability surpass those of Path 1.

Red dots represent non-optimal objective values and blue diamonds represent optimal values.

4.3. Limitations

Our study has limitations that need to be acknowledged. First, the effectiveness of the optimization process heavily depends on the selection of constraint conditions, requiring expert decision-making and significant labor investment. Consequently, the optimization outcomes may vary considerably under different constraint settings. Currently, the application of optimization techniques in urban research is relatively limited, highlighting the need for gradual standardization in future studies. Second, while we evaluated the HVI before and after optimization to assess the impact, using average values to represent the overall performance of HVI for a specific LCZ may not provide sufficient accuracy. In future research, it is important to consider the inherent randomness of real-world environments by incorporating techniques such as Monte Carlo algorithms to better simulate the optimized HVI in practical scenarios. Furthermore, our current research primarily focuses on the characteristics of LCZ and HVI without delving into the underlying reasons, driving forces, or the coupling factors associated with these features. A more in-depth exploration of these aspects is crucial for a comprehensive understanding of the phenomenon. Lastly, the present combination of HVI and LCZ optimization mainly concentrates on spatial configuration, neglecting temporal characteristics. Throughout

the timeline of urban development, the distribution of LCZ types undergoes a series of changes, and its relationship with HVI has yet to be explored. Future research should aim to develop new data sources or employ innovative technical methods to address these aforementioned limitations and advance the field.

5. Conclusions

Based on our analysis approach and findings, we have drawn the following conclusions:

- (1) The performance of different LCZs varied across the three sub-dimensions of HVI. Building LCZs generally showed higher levels of thermal exposure compared to natural LCZs. Among the LCZs, LCZ2 exhibited the highest thermal exposure value (0.567), while the lowest value was observed in LCZG (0.212). LCZ1 had the highest thermal sensitivity value (0.504), whereas LCZA had the lowest (0.158). In terms of adaptability, the spatial characteristics differed from exposure and sensitivity. Lower adaptability values were observed at the edge of the study area and in the circular area outside the center. Building LCZs generally had higher adaptability at middle and upper levels compared to natural LCZs, while the adaptability of low-rise LCZs was lower than that of natural LCZs. LCZ2 (0.383) and LCZ1 (0.365) had the highest HVI values, while LCZ3 (0.250) had the lowest.
- (2) Overall, LCZ1 (0.668) and LCZ2 (0.612) exhibited extremely high HVI, while LCZ3 (0.536), LCZ8 (0.515), LCZ5 (0.501), and LCZ4 (0.491) showed high HVI. Building LCZs had higher HVI than natural LCZs, with the lowest HVI observed in LCZG. The compact type LCZ had higher HVI than LCZ8 and the open type. The distribution proportion of HVI varied across different levels within the LCZs. For LCZ1 and LCZ2, over 90 % of the area exhibited extremely high and high HVI. The internal distribution of HVI within LCZ8 showed the greatest variation.
- (3) Before optimization, the overall thermal fragility value in the research area was 49,034.67. However, after optimization, this value decreased to 41,772.37, representing a reduction of 14.81 %. These findings demonstrate that the linearly weighted multi-objective optimization model can help cities reduce thermal fragility. Under the control of minimizing thermal fragility and LCZ area variation objectives, along with related constraints, the optimization scheme primarily increased the areas of LCZ4, LCZ5, LCZA, and LCZD, while reducing the areas of LCZ6, LCZ8, LCZ1, and LCZ2. As a result of the optimization, LCZ4 exhibited the highest population-carrying capacity.

These conclusions, in conjunction with urban planning considerations, can be applied to optimize the urban environment in practical applications.

Declaration of Competing Interest

The authors declare that they have no known competing financial interests or personal relationships that could have appeared to influence the work reported in this paper.

Data availability

Data will be made available on request.

Acknowledgements

This research study was supported by the National Natural Science Foundation of China (grant no's 41771178, 42030409, and 41671151), Basic Scientific Research Project (Key Project) of the Education

Department of Liaoning Province (grant no. LJKZ0964), the Fundamental Research Funds for the Central Universities (grant no. N2111003), Natural Science Foundation of Guizhou Province (grant no. (2019)1150).

References

- Aroca-Jimenez, E., et al. (2020). How to construct and validate an integrated socio-economic vulnerability index: Implementation at regional scale in urban areas prone to flash flooding. *Science Total Environment*, 746, Article 140905. <https://doi.org/10.1016/j.scitotenv.2020.140905>
- Cai, Z., et al. (2021). A cooled city? Comparing human activity changes on the impact of urban thermal environment before and after city-wide lockdown. *Building and Environment*, 195. <https://doi.org/10.1016/j.buildenv.2021.107729>
- Chang, Y., et al. (2021). Exploring diurnal thermal variations in urban local climate zones with ECOSTRESS land surface temperature data. *Remote Sensing of Environment*, 263. <https://doi.org/10.1016/j.rse.2021.112544>
- Chen, B., et al. (2022a). Diurnal heat exposure risk mapping and related governance zoning: A case study of Beijing, China. *Sustainable Cities and Society*, 81. <https://doi.org/10.1016/j.scs.2022.103831>
- Chen, Q., et al. (2018). Spatially explicit assessment of heat health risk by using multi-sensor remote sensing images and socioeconomic data in Yangtze River Delta, China. *International Journal of Health Geographics*, 17(1), 15. <https://doi.org/10.1186/s12942-018-0135-y>
- Chen, T. L., et al. (2022b). Heat vulnerability and extreme heat risk at the metropolitan scale: A case study of Taipei metropolitan area, Taiwan. *Urban Climate*, 41. <https://doi.org/10.1016/j.uclim.2021.101054>
- Chen, Y., et al. (2023a). Relationship between urban spatial form and seasonal land surface temperature under different grid scales. *Sustainable Cities and Society*, 89. <https://doi.org/10.1016/j.scs.2022.104374>
- Chen, Y., et al. (2023b). Spatial and temporal characteristics of nighttime UHII based on local climate zone scheme using mobile measurement-A case study of Changsha. *Building and Environment*, 228. <https://doi.org/10.1016/j.buildenv.2022.109869>
- Demuzere, M., et al. (2022). A global map of local climate zones to support earth system modelling and urban-scale environmental science. *Earth System Science Data*, 14(8), 3835–3873. <https://doi.org/10.5194/essd-14-3835-2022>
- Dong, W., et al. (2015). New climate and socio-economic scenarios for assessing global human health challenges due to heat risk. *Climatic Change*, 130(4), 505–518. <https://doi.org/10.1007/s10584-015-1372-8>
- Du, H. Y., et al. (2017). Quantifying the cool island effects of urban green spaces using remote sensing Data. *Urban Forestry & Urban Greening*, 27, 24–31. <https://doi.org/10.1016/j.ufug.2017.06.008>
- Ebi, K. L., et al. (2021). Hot weather and heat extremes: health risks. *The Lancet*, 398(10301), 698–708. [https://doi.org/10.1016/s0140-6736\(21\)01208-3](https://doi.org/10.1016/s0140-6736(21)01208-3)
- El-Zein, A., & Tonmoy, F. N. (2015). Assessment of vulnerability to climate change using a multi-criteria outranking approach with application to heat stress in Sydney. *Ecological Indicators*, 48, 207–217. <https://doi.org/10.1016/j.ecolind.2014.08.012>
- Ellena, M., et al. (2020). The heat-health nexus in the urban context: A systematic literature review exploring the socio-economic vulnerabilities and built environment characteristics. *Urban Climate*, 34. <https://doi.org/10.1016/j.uclim.2020.100676>
- Estoque, R. C., et al. (2020). Heat health risk assessment in Philippine cities using remotely sensed data and social-ecological indicators. *Nature Communications*, 11(1), 1581. <https://doi.org/10.1038/s41467-020-15218-8>
- Fischer, E., et al. (2022). A risk index for assessing heat stress mitigation strategies. An application in the Mediterranean context. *Journal of Cleaner Production*, 346. <https://doi.org/10.1016/j.jclepro.2022.131210>
- Ford, J. D., et al. (2018). Vulnerability and its discontents: the past, present, and future of climate change vulnerability research. *Climatic Change*, 151(2), 189–203. <https://doi.org/10.1007/s10584-018-2304-1>
- Gardes, T., et al. (2020). Statistical prediction of the nocturnal urban heat island intensity based on urban morphology and geographical factors - An investigation based on numerical model results for a large ensemble of French cities. *Science of the Total Environment*, 737, Article 139253. <https://doi.org/10.1016/j.scitotenv.2020.139253>
- Giannaros, C., et al. (2022). The extreme heat wave of July-August 2021 in the Athens urban area (Greece): Atmospheric and human-biometeorological analysis exploiting ultra-high resolution numerical modeling and the local climate zone framework. *Science of the Total Environment*, Article 159300. <https://doi.org/10.1016/j.scitotenv.2022.159300>
- Guo, X., et al. (2019). Estimating fine-scale heat vulnerability in Beijing through two approaches: Spatial patterns, similarities, and divergence. *Remote Sensing*, 11(20). <https://doi.org/10.3390/rs11202358>
- Han, B., et al. (2022). Using local climate Zones to investigate Spatio-temporal evolution of thermal environment at the urban regional level: A case study in Xi'an, China. *Sustainable Cities and Society*, 76. <https://doi.org/10.1016/j.scs.2021.103495>
- He, C., et al. (2019). Exploring the mechanisms of heat wave vulnerability at the urban scale based on the application of big data and artificial societies. *Environment International*, 127, 573–583. <https://doi.org/10.1016/j.envint.2019.01.057>
- Ho, H. C., et al. (2018). Spatiotemporal analysis of regional socio-economic vulnerability change associated with heat risks in Canada. *Applied Geography*, 95, 61–70. <https://doi.org/10.1016/j.apgeog.2018.04.015>
- Huang, X., et al. (2020). High-resolution urban land-cover mapping and landscape analysis of the 42 major cities in China using ZY-3 satellite images. *Science Bulletin*, 65(12), 1039–1048. <https://doi.org/10.1016/j.scib.2020.03.003>
- Inostroza, L., et al. (2016). A heat vulnerability index: spatial patterns of exposure, sensitivity and adaptive capacity for santiago de chile. *PLoS One*, 11(9), Article e0162464. <https://doi.org/10.1371/journal.pone.0162464>
- IPCC Climate Change. (2022). *Impacts, adaptation, and vulnerability. Contribution of working group II to the sixth assessment report of the intergovernmental panel on climate change.*
- IPCC Climate Change. (2007). *Impacts, adaptation and vulnerability: Contribution of working group II to the fourth assessment report of the intergovernmental panel on climate change.*
- Jiang, Y., et al. (2015). Downscaling GOES land surface temperature for assessing heat wave health risks. *IEEE Geoscience and Remote Sensing Letters*, 12(8), 1605–1609. <https://doi.org/10.1109/lgrs.2015.2414897>
- Kabano, P., et al. (2021). Evidence of urban heat island impacts on the vegetation growing season length in a tropical city. *Landscape and Urban Planning*, 206. <https://doi.org/10.1016/j.landurbplan.2020.103989>
- Karanja, J., & Kiage, L. (2021). Perspectives on spatial representation of urban heat vulnerability. *Science of The Total Environment*, 774. <https://doi.org/10.1016/j.scitotenv.2021.145634>
- Kothakar, R., et al. (2022). Approach to local climate zone based energy consumption assessment in an Indian city. *Energy and Buildings*, 259. <https://doi.org/10.1016/j.enbuild.2022.111835>
- Lau, K. K. L., et al. (2019). Outdoor thermal comfort in different urban settings of sub-tropical high-density cities: An approach of adopting local climate zone (LCZ) classification. *Building and Environment*, 154, 227–238. <https://doi.org/10.1016/j.buildenv.2019.03.005>
- Leconte, F., et al. (2015). Using Local Climate Zone scheme for UHI assessment: Evaluation of the method using mobile measurements. *Building and Environment*, 83, 39–49. <https://doi.org/10.1016/j.buildenv.2014.05.005>
- Lemoine-Rodriguez, R., et al. (2022). Does urban climate follow urban form? Analysing intraurban LST trajectories versus urban form trends in 3 cities with different background climates. *Science Total Environment*, 830, Article 154570. <https://doi.org/10.1016/j.scitotenv.2022.154570>
- Li, D., et al. (2015). Contrasting responses of urban and rural surface energy budgets to heat waves explain synergies between urban heat islands and heat waves. *Environmental Research Letters*, 10(5). <https://doi.org/10.1088/1748-9326/10/5/054009>
- Li, L., et al. (2022a). Variabilities of land surface temperature and frontal area index based on local climate zone. *IEEE Journal of Selected Topics in Applied Earth Observations and Remote Sensing*, 15, 2166–2174. <https://doi.org/10.1109/jstars.2022.3153958>
- Li, N., et al. (2021). Urban thermal characteristics of local climate zones and their mitigation measures across cities in different climate zones of China. *Remote Sensing*, 13(8). <https://doi.org/10.3390/rs13081468>
- Li, X., et al. (2022b). The role of blue green infrastructure in the urban thermal environment across seasons and local climate zones in East Africa. *Sustainable Cities and Society*, 80. <https://doi.org/10.1016/j.scs.2022.103798>
- LINDO Systems. (2023). LINGO 18 includes a wide range of performance enhancements and new features. Retrieved from <https://www.lindo.com/index.php/ls-download/s/try-lingo/>. Accessed April 13, 2023.
- Liu, Y., et al. (2021a). The turning point between urban vegetation and artificial surfaces for their competitive effect on land surface temperature. *Journal of Cleaner Production*, 292. <https://doi.org/10.1016/j.jclepro.2021.126034>
- Liu, Z., et al. (2021b). Challenges and opportunities for carbon neutrality in China. *Nature Reviews Earth & Environment*. <https://doi.org/10.1038/s43017-021-00244-x>
- Mohammad Harmay, N. S., & Choi, M. (2022). Effects of heat waves on urban warming across different urban morphologies and climate zones. *Building and Environment*, 209. <https://doi.org/10.1016/j.buildenv.2021.108677>
- Nayak, S. G., et al. (2018). Development of a heat vulnerability index for New York State. *Public Health*, 161, 127–137. <https://doi.org/10.1016/j.puhe.2017.09.006>
- Oke, T. R., & Stewart, I. D. (2012). Local climate zones for urban temperature studies. *Bulletin of the American Meteorological Society*, 93(12), 1879–1900. <https://doi.org/10.1175/bams-d-11-00019.1>
- Pappalardo, L., et al. (2015). Returners and explorers dichotomy in human mobility. *Nature Communications*, 6, 8166. <https://doi.org/10.1038/ncomms9166>
- Peng, J., et al. (2020). How to effectively mitigate urban heat island effect? A perspective of waterbody patch size threshold. *Landscape and Urban Planning*, 202. <https://doi.org/10.1016/j.landurbplan.2020.103873>
- Qin, Z. h., et al. (2001). Mono-window algorithm for retrieving land surface temperature from Landsat TM6 data. *Acta Geographica Sinica*, 56(4), 456–466. <https://doi.org/10.11821/xb200104009>
- Renc, A., et al. (2022). Spatial structure of the surface heat and cold islands in summer based on Landsat 8 imagery in southern Poland. *Ecological Indicators*, 142. <https://doi.org/10.1016/j.ecolind.2022.109181>
- Russo, S., et al. (2014). Magnitude of extreme heat waves in present climate and their projection in a warming world. *Journal of Geophysical Research: Atmospheres*, 119(22). <https://doi.org/10.1002/2014jd022098>
- Sabrin, S., et al. (2020). Quantifying environmental and social vulnerability: Role of urban Heat Island and air quality, a case study of Camden, NJ. *Urban Climate*, 34. <https://doi.org/10.1016/j.uclim.2020.100699>
- Schwaab, J., et al. (2021). The role of urban trees in reducing land surface temperatures in European cities. *Nature Communications*, 12(1), 6763. <https://doi.org/10.1038/s41467-021-26768-w>
- Song, J., et al. (2020). Fine-scale mapping of an evidence-based heat health risk index for high-density cities: Hong Kong as a case study. *Science Total Environment*, 718, Article 137226. <https://doi.org/10.1016/j.scitotenv.2020.137226>

- Spinoni, J., et al. (2015). Heat and cold waves trends in the Carpathian Region from 1961 to 2010. *International Journal of Climatology*, 35(14), 4197–4209. <https://doi.org/10.1002/joc.4279>
- Stewart, I. D., et al. (2014). Evaluation of the 'local climate zone' scheme using temperature observations and model simulations. *International Journal of Climatology*, 34(4), 1062–1080. <https://doi.org/10.1002/joc.3746>
- Sun, X., et al. (2014). Heat wave impact on mortality in Pudong New Area, China in 2013. *Science Total Environment*, 493, 789–794. <https://doi.org/10.1016/j.scitotenv.2014.06.042>
- Sun, Y., et al. (2022). Mapping urban socio-economic vulnerability related to heat risk: A grid-based assessment framework by combing the geospatial big data. *Urban Climate*, 43. <https://doi.org/10.1016/j.uclim.2022.101169>
- Tomlinson, C. J., et al. (2011). Including the urban heat island in spatial heat health risk assessment strategies: a case study for Birmingham, UK. *International Journal of Health Geographics*, 10, 42. <https://doi.org/10.1186/1476-072X-10-42>
- Tucker, C. J., et al. (1985). Satellite remote sensing of total herbaceous biomass production in the senegalese sahel: 1980–1984. *Remote Sensing of Environment*, 17(3), 233–249. [https://doi.org/10.1016/0034-4257\(85\)90097-5](https://doi.org/10.1016/0034-4257(85)90097-5)
- Tuholske, C., et al. (2021). Global urban population exposure to extreme heat. *Proceedings of the National Academy of Sciences of the United States of America*, 118(41). <https://doi.org/10.1073/pnas.2024792118>
- Wang, J., et al. (2023). Comparing relationships between urban heat exposure, ecological structure, and socio-economic patterns in Beijing and New York City. *Landscape and Urban Planning*, 235. <https://doi.org/10.1016/j.landurbplan.2023.104750>
- Wu, J., et al. (2022). Analysis of Spatio-temporal patterns and related factors of thermal comfort in subtropical coastal cities based on local climate zones. *Building and Environment*, 207. <https://doi.org/10.1016/j.buildenv.2021.108568>
- Wu, W., et al. (2021). Seasonal variation in the effects of urban environmental factors on land surface temperature in a winter city. *Journal of Cleaner Production*, 299. <https://doi.org/10.1016/j.jclepro.2021.126897>
- Xiang, Z., et al. (2022). Heat vulnerability caused by physical and social conditions in a mountainous megacity of Chongqing, China. *Sustainable Cities and Society*, 80. <https://doi.org/10.1016/j.scs.2022.103792>
- Xu, H. Q. (2006). Modification of normalised difference water index (NDWI) to enhance open water features in remotely sensed imagery. *International Journal of Remote Sensing*, 27(14), 3025–3033. <https://doi.org/10.1080/01431160600589179>
- Yang, X., et al. (2018). Assessing the thermal behavior of different local climate zones in the Nanjing metropolis, China. *Building and Environment*, 137, 171–184. <https://doi.org/10.1016/j.buildenv.2018.04.009>
- Yang, J., et al. (2019). Local climate zone ventilation and urban land surface temperatures: Towards a performance-based and wind-sensitive planning proposal in megacities. *Sustainable Cities and Society*, 47. <https://doi.org/10.1016/j.scs.2019.101487>
- Yang, J., et al. (2021a). Understanding land surface temperature impact factors based on local climate zones. *Sustainable Cities and Society*, 69. <https://doi.org/10.1016/j.scs.2021.102818>
- Yang, J., et al. (2020a). Optimizing local climate zones to mitigate urban heat island effect in human settlements. *Journal of Cleaner Production*, 275. <https://doi.org/10.1016/j.jclepro.2020.123767>
- Yang, J., et al. (2020b). Investigating the diversity of land surface temperature characteristics in different scale cities based on local climate zones. *Urban Climate*, 34. <https://doi.org/10.1016/j.uclim.2020.100700>
- Yang, J., et al. (2021b). Projecting heat-related excess mortality under climate change scenarios in China. *Nature Communications*, 12(1), 1039. <https://doi.org/10.1038/s41467-021-21305-1>
- Yazar, M., et al. (2022). Adaptation, exposure, and politics: Local extreme heat and global climate change risk perceptions in the phoenix metropolitan region, USA. *Cities*, 127. <https://doi.org/10.1016/j.cities.2022.103763>
- Yi, C., et al. (2022). Spatial temperature differences in local climate zones of Seoul metropolitan area during a heatwave. *Urban Climate*, 41. <https://doi.org/10.1016/j.uclim.2021.101012>
- Zha, Y., et al. (2003). Use of normalized difference built-up index in automatically mapping urban areas from TM imagery. *International Journal of Remote Sensing*, 24(3), 583–594. <https://doi.org/10.1080/01431160304987>
- Zhang, R., et al. (2022). Warming and cooling effects of local climate zones on urban thermal environment. *Front Public Health*, 10, Article 1072174. <https://doi.org/10.3389/fpubh.2022.1072174>
- Zhi, Y., et al. (2020). Analysis of land surface temperature driving factors and spatial heterogeneity research based on geographically weighted regression model. *Complexity*, 2020, 1–9. <https://doi.org/10.1155/2020/2862917>
- Zhou, L., et al. (2022). Understanding the effects of 2D/3D urban morphology on land surface temperature based on local climate zones. *Building and Environment*, 208. <https://doi.org/10.1016/j.buildenv.2021.108578>
- Zhou, Y., et al. (2021). Mapping local climate zones and their associated heat risk issues in Beijing: Based on open data. *Sustainable Cities and Society*, 74. <https://doi.org/10.1016/j.scs.2021.103174>